Mitigation of third-order resonances in the Fermilab Recycler Ring

Cristhian Gonzalez-Ortiz[*] and Robert Ainsworth
Fermi National Accelerator Laboratory, Batavia, Illinois 60510, USA

Peter Ostroumov[†]
Department of Physics and Astronomy, Michigan State University, East Lansing, Michigan 48824, USA

(Received 28 January 2025; accepted 15 April 2026; published 29 May 2026)

As the Fermilab accelerator complex prepares for higher-intensity operation under the Proton Improvement Plan II (PIP-II), addressing the negative impacts of third-order resonance becomes crucial for the Recycler Ring (RR). Minimizing fluctuations of third-order resonance driving terms (RDTs) around the ring allows one to enhance dynamic aperture and reduce resonance-driven losses. This work experimentally demonstrates a mitigation scheme using normal and skew sextupoles, optimized via the response matrix method, in order to manipulate and minimize RDTs for a hadron storage ring. Furthermore, the effectiveness of this approach for a bunched beam at high intensities is evaluated through dynamic and static tune scans. The results show that resonance compensation remains effective in the presence of space charge, reducing beam loss and emittance growth compared to uncompensated operation. These new measurements extend previous observations of third-order resonance effects in high-intensity bunched beams by explicitly quantifying beam loss, emittance growth, and tail population under conditions where the RDTs are minimized around the ring. Overall, these findings strengthen the applicability of resonance control in the RR and highlight its importance for reliable high-intensity operation in the PIP-II era.

DOI: 10.1103/7qs8-3zl4

I. INTRODUCTION

The Recycler Ring (RR) is a permanent-magnet storage ring in the Fermilab accelerator complex that stores bunched protons at a fixed energy of 8 GeV [1]. It shares the 3.3 km tunnel with the main injector (MI), where protons from the RR are accelerated to 120 GeV for delivery to the NuMI experiment [2–5]. For high-intensity operation, the RR slip-stacks booster batches to double the stored intensity before transfer to the MI. A key feature of the RR lattice is the use of combined-function permanent magnets. Although designed to provide only dipole and quadrupole fields, construction tolerances introduce sextupole components distributed around the ring with a superperiodicity of two. These systematic sextupole fields are expected to be the dominant drivers of third-order resonances, a central topic of this work.

The Proton Improvement Plan II (PIP-II) will establish the Fermilab complex as a multi-MW proton facility [6]. Its near-term goal is to deliver a 1.2 MW proton beam to the Deep Underground Neutrino Experiment (DUNE) via the Long-Baseline Neutrino Facility (LBNF). This requires a new 800 MeV superconducting linac, upgrades to the booster, and modest improvements to the MI and RR, enabling a 50% increase in particles per pulse. Figure 1 shows the upgraded complex, and Table I lists nominal parameters for PIP-II operation, including higher bunch intensities, a shorter MI ramp, and a faster booster cycle.

As RR intensities increase, mitigating space-charge detuning effects becomes essential. Space charge introduces incoherent tune shifts, with core particles experiencing the strongest force and creating a tune spread. Figure 2 shows a PySCRDT [7,8] calculation of the tune footprint for 1×10^{11} protons per bunch, giving a tune shift of about 0.09 in both planes under PIP-II conditions. Here Q_x and Q_y denote the horizontal and vertical betatron tunes. At the nominal working point, the beam distribution may be subject to emittance growth and potential beam loss induced by nearby third-order resonances in the tune diagram, in particular the normal lines $3Q_x = 76$ and $Q_x + 2Q_y = 74$, as well as the skew lines $3Q_y = 73$ and $2Q_x + Q_y = 75$. The impact of these nearby third-order resonances on beam loss and emittance growth is studied quantitatively in the present work.

[*]Contact author: gonza839@fnal.gov
[†]Also at Facility for Rare Isotope Beams (FRIB), Michigan State University, East Lansing, Michigan 48824, USA.

Published by the American Physical Society under the terms of the Creative Commons Attribution 4.0 International license. Further distribution of this work must maintain attribution to the author(s) and the published article's title, journal citation, and DOI.

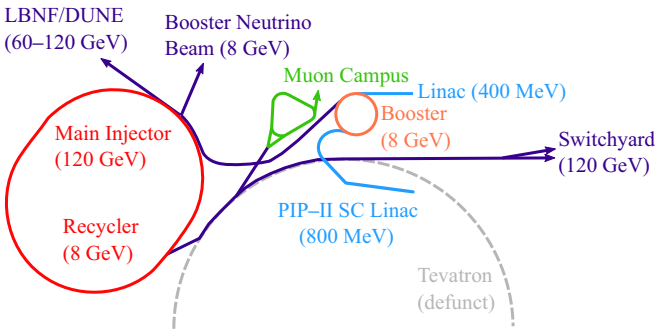


FIG. 1. Future layout of the Fermilab accelerator complex for the Proton Improvement Plan II (PIP-II).

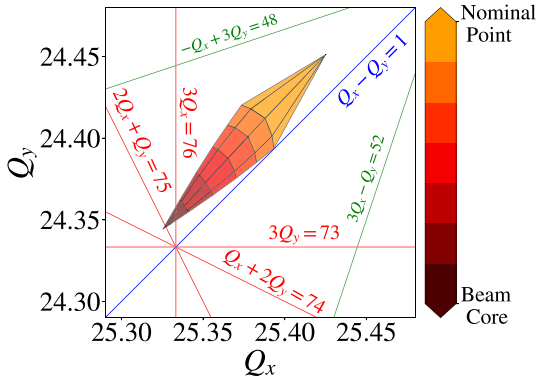


FIG. 2. Space charge tune footprint calculated using PySCRDT [7] for 1×10^{11} particles per bunch in a PIP-II Recycler Ring.

Performance limitations from low-order resonances and space-charge-driven tune shifts are common across high-intensity hadron accelerators worldwide. Third-order resonance compensation optics have been studied in synchrotrons at CERN [9–12], J-PARC [13], and GSI [14–16], while simulation studies have investigated space-charge limits in heavy-ion machines [17]. Minimization or cancellation of resonance driving terms (RDTs) is a well-established method [18–22] to enlarge the dynamic aperture and suppress resonance-driven losses. Building on these efforts, the present work experimentally demonstrates resonance compensation in the Fermilab Recycler Ring, extending to conditions with significant space-charge tune spread relevant to PIP-II and other future high-intensity programs. Because the combined-function permanent magnets in the recycler introduce systematic sextupole components that dominate third-order resonances, our study focuses on their compensation through RDT minimization. We present detailed measurements that verify compensation, explore performance at high intensity, and characterize the interplay between space-charge tune spread and compensated resonance lines.

TABLE I. Typical Recycler Ring properties for beam sent to NuMI, with some PIP-II nominal parameters.

Parameter	Value	Unit
Circumference	3319.4	m
Momentum	8.835	GeV/c
Revolution period	11.1	μs
Revolution frequency	89.6	kHz
rf frequency	52.8	MHz
rf voltage	80	kV
	140 (PIP-II)	kV
Harmonic number	588	
Synchrotron tune	0.0028	
	0.0038 (PIP-II)	
Slip factor	-8.6×10^{-3}	
Superperiodicity	2	
Horizontal tune	25.43	
Vertical tune	24.445	
Horizontal chromaticity	−6	
Vertical chromaticity	−7	
Transverse acceptance	40	π mm mrad
95% normalized emittance	15	π mm mrad
95% longitudinal emittance	0.08	eV s
rms $\delta p/p$	0.0004	
Intensity	5×10^{10}	ppb
	8×10^{10} (PIP-II)	ppb
MI ramp time	1.2	s
	1.133	s
	1.067	s
Booster frequency	15	Hz
	20 (PIP-II)	Hz

II. COMPENSATION AT LOW INTENSITIES

A. The Recycler Ring

The Recycler Ring (RR) is a permanent-magnet storage ring operating at a fixed momentum of 8.835 GeV/c (8 GeV beam energy). Its lattice consists of 104 FODO cells with a 90° phase advance, arranged with a superperiodicity of two [1,3–5]. Despite the use of fixed-field magnets, tune flexibility is provided by dedicated tune trombones—linear quadrupole inserts that introduce controlled local phase advances while preserving the Twiss parameters at the boundaries of the insertion (matching points) [1,3,23]. This configuration allows independent adjustment of both horizontal and vertical tunes within a range of $\Delta Q_u = \pm 0.5$.

In the Recycler Ring, sextupole fields originate from the chromatic sextupoles, the compensation sextupoles, and the permanent-magnet elements. Chromaticity can be varied between −5 and −20 in both planes using dedicated sextupole circuits [3], while compensation sextupoles are installed specifically for resonance mitigation [4]. The dominant drivers of third-order resonances, however, are the permanent combined-function magnets. Although designed as dipole-quadrupole elements, construction tolerances introduce systematic sextupole components that strongly excite third-order resonance lines. Contributions

from chromatic sextupoles are comparatively minor, making the RR's resonance behavior largely systematic (structural) rather than error-driven.

The Recycler Ring is instrumented with 208 beam position monitors (BPMs), comprising 104 horizontal and 104 vertical devices distributed around the lattice. These BPMs provide turn-by-turn data that are used for tune determination and spectral analysis. In addition, the machine is equipped with a horizontal and a vertical ionization profile monitor (IPM), which measure the corresponding transverse beam profiles and emittances [24].

B. Third-order RDTs and resonance lines

The condition for resonance lines can be written as

$$(j-k)Q_x + (l-m)Q_y = p, \tag{1}$$

where j, k, l, m, and p are non-negative integers. In this work, we are particularly concerned with third-order resonances, i.e., $j+k+l+m=3$. Figure 3 shows the theoretical positions of the main resonances overlaid on an experimental dynamic loss map. In addition to the dominant third-order resonances, fourth- and even traces of fifth-order resonance lines are discernible, with the third-order lines exhibiting the greatest prominence.

The loss maps were constructed with low-intensity beam following the procedure described in Ref. [4], in which losses from two complementary scans are interpolated. In one case, the horizontal tune is varied dynamically from 25.46 to 25.32 at several fixed vertical tunes, while in the other case, the vertical tune is varied from 24.46 to 24.32 at several fixed horizontal tunes. The set tunes in the control system are derived from the model's tune trombone coefficients and the applied quadrupole currents and are further calibrated using low-intensity turn-by-turn measurements. We note that the tune scans are performed using a localized tune trombone, which might break the superperiodicity of the ring; any additional effects associated with this tune-scanning procedure are acknowledged but not examined further, as they are beyond the scope of the present study.

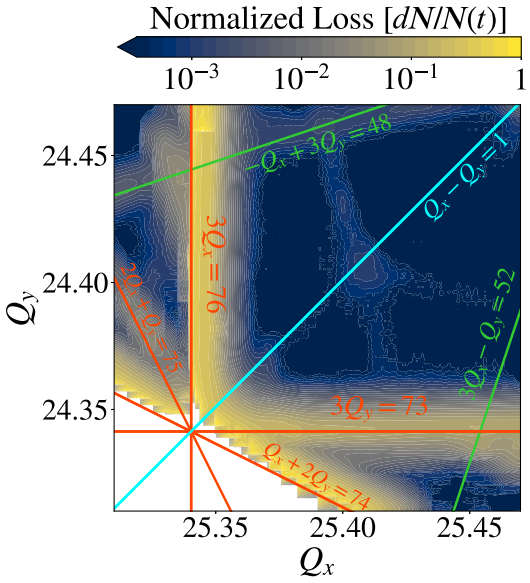


FIG. 3. Experimental dynamic loss map from low-intensity horizontal and vertical tune scans, with theoretical resonance lines overlaid. The tune scans were performed in the leftward and downward directions by dynamically decreasing the focusing strength of the trombone quadrupoles. The color scale shows normalized beam losses, with yellow indicating higher loss rates and white marking regions without beam data.

The resonance stop band width is defined as the range in tune space over which a resonance significantly perturbs particle motion and produces measurable beam loss. It depends on the strength of the resonance driving terms (RDTs) as well as beam parameters, and is visible in Fig. 3 as the yellow regions of the color map. While loss maps provide a powerful tool to visualize resonances and estimate their stop band widths, their features can also depend on experimental details such as the scan direction and the evolving beam distribution. For example, the $3Q_x = 76$ resonance is sufficiently strong that, during a horizontal tune scan, only approximately 5% of the beam survives, which limits the sensitivity to adjacent weaker resonances such as $2Q_x + Q_y = 75$. To mitigate such effects, the loss map in Fig. 3 presents normalized losses and masks regions without available beam data in white.

Resonance driving terms (RDTs) allow one to quantify the strength of a resonance. The RDTs h_{jklm} are defined by the order in which they enter the one-turn normal form Hamiltonian [20,25]. With the assumption of thin elements around the ring, the general expression to define RDTs reads:

$$h_{jklm} = \Xi_{jklm} \sum_u L_u K_{n-1,u} \beta_{x,u}^{\frac{j+k}{2}} \beta_{y,u}^{\frac{l+m}{2}} e^{i[(j-k)\phi_{x,u} + (l-m)\phi_{y,u}]}, \tag{2}$$

where Ξ_{jklm} is just a constant defined as

$$\Xi_{jklm} = -\frac{1}{2^n}\frac{1}{n!}\binom{n}{l+m}\binom{j+k}{j}\binom{l+m}{l}. \tag{3}$$

For Eqs. (2) and (3), $n = j+k+l+m$ represents the order of the RDT. The sum over u is taken over all multipoles of order n and length L_u that either have a normal component $K_{n-1,u}$ if $l+m$ is even, or a skew component $K_{n-1,u} = K_{n-1,u}^{(s)}$ if $l+m$ is odd. The symbols for $\beta_{x,u}$, $\beta_{y,u}$, $\phi_{x,u}$, and $\phi_{y,u}$ represent the unperturbed beta functions and phase advances in each plane, respectively. Table II summarizes the third-order RDTs of relevance to this work.

The generating function coefficients (GFCs) f_{jklm} are related to their RDTs h_{jklm} by the following expression:

TABLE II. Corresponding RDTs for each resonance line with the spectral location $Q(\ldots)$ of their horizontal spectral lines (HSL) and vertical spectral lines (VSL).

Resonance line	Source	RDT expression	Q (HSL)	Q (VSL)
$3Q_x = 76$	Normal sextupole	$h_{3000} = -\frac{1}{48}\sum_u K_{2,u} L_u \beta_{x,u}^{\frac{3}{2}} e^{3i\phi_{x,u}}$	$-2Q_x$	
$Q_x + 2Q_y = 74$	Normal sextupole	$h_{1020} = -\frac{1}{16}\sum_u K_{2,u} L_u \beta_{x,u}^{\frac{1}{2}} \beta_{y,u} e^{i[\phi_{x,u}+2\phi_{y,u}]}$	$-2Q_y$	$-Q_x - Q_y$
$3Q_y = 73$	Skew sextupole	$h_{0030} = -\frac{1}{48}\sum_u K_{2,u}^{(s)} L_u \beta_{y,u}^{\frac{3}{2}} e^{3i\phi_{y,u}}$		$-2Q_y$
$2Q_x + Q_y = 75$	Skew sextupole	$h_{2010} = -\frac{1}{16}\sum_u K_{2,u}^{(s)} L_u \beta_{x,u} \beta_{y,u}^{\frac{1}{2}} e^{i[2\phi_{x,u}+\phi_{y,u}]}$	$-Q_x - Q_y$	$-2Q_x$

$$f_{jklm} = \frac{h_{jklm}}{1 - e^{2\pi i[(j-k)Q_x + (l-m)Q_y]}}. \quad (4)$$

Figure 4 shows the lattice-model calculation of the third-order resonance driving terms (RDTs) h_{3000}, h_{1020}, h_{0030}, and h_{2010} using the MAD-X PTC module [26]. These results correspond to the bare-machine configuration, i.e., with the trombone quadrupoles [23] and chromatic sextupoles [27] switched off. The local variations and discontinuities in the RDTs reflect the spatial distribution of sextupole fields around the lattice, as discussed in Refs. [18–20]. Also shown are the contributions from individual sextupole components, expressed as the normal $k_2 L$ and skew $k_2^{(s)} L$ values for each lattice element. The normal sextupole strengths $k_2 L$ exhibit a pronounced lattice-periodic (systematic) pattern around the ring, whereas the skew components $k_2^{(s)} L$ appear predominantly as nonsystematic variations about a small mean value and are nearly an order of magnitude smaller.

The combined-function permanent magnets are the primary source of the systematic (normal) sextupole fields. Because these magnets are arranged with an approximate superperiodicity $S = 2$, the corresponding sextupole distribution contains mainly structural harmonics compatible with this symmetry. In particular, for structural resonances the driving harmonic index satisfies $p = rS$ with integer r, and the dominant normal third-order lines studied here —$3Q_x = 76$ and $Q_x + 2Q_y = 74$—are consistent with this condition since 76 and 74 are multiples of $S = 2$. In contrast, the skew third-order terms are primarily driven by nonsystematic skew sextupole components and are therefore expected to be weaker and dominated by random harmonics rather than by structural contributions.

The RDT calculations are based on a thin-element lattice model that incorporates a detailed component list and measured magnet coefficients closely matched to those in the tunnel. The results correspond to on-momentum particles, with the relative β-function error between model and measurement below 10% in the horizontal plane and 5% in the vertical [5]. Figure 4 shows the calculated RDTs listed in Table II for all beam position monitors (BPMs) around the ring. The normal sextupole terms h_{3000} ($3Q_x = 76$) and h_{1020} ($Q_x + 2Q_y = 74$) exhibit the largest amplitudes, consistent with the dynamic loss map in Fig. 3, where these resonances drive the strongest losses, particularly $3Q_x$. The skew sextupole terms h_{0030} and h_{2010}

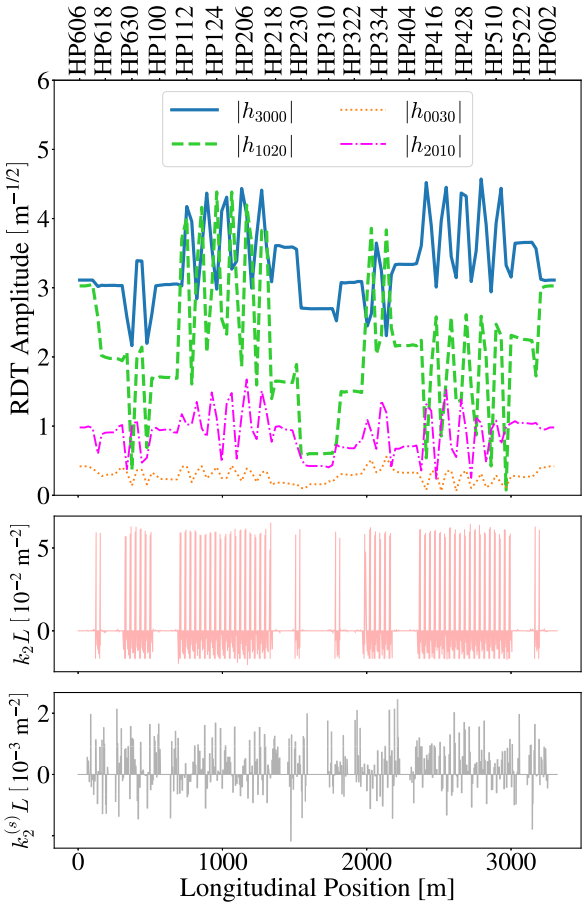


FIG. 4. Lattice-model calculation of the relevant third-order RDTs, i.e., h_{3000}, h_{1020}, h_{0030}, and h_{2010}, around the ring from an arbitrary starting point as calculated from the lattice model using the MAD-X PTC module. Each label in the upper axis (e.g., HP606, HP620, ... , HP514) corresponds to a different horizontal BPM in the accelerator.

originate from nonsystematic variations of the skew sextupole component $k_2^{(s)}L$ and are much smaller in amplitude.

While the model predicts h_{0030} to be weaker than h_{2010}, the loss map from Fig. 3 shows the opposite trend, with the $3Q_y = 73$ resonance appearing stronger than the $2Q_x + Q_y = 75$ line. This difference reflects the finite resolution of dynamic tune-scan loss maps after substantial beam depletion. Loss rates are normalized to the instantaneous intensity, and data points below 1% of the initial intensity are excluded to avoid artificial amplification when the remaining beam population is negligible. Because the horizontal downward scan loses ~95% of the intensity at $3Q_x = 76$, the sensitivity to weaker features encountered at lower Q_x (e.g., $2Q_x + Q_y = 75$) is reduced, and this limitation propagates into combined maps that incorporate both horizontal and vertical scans. Thus, loss maps provide a robust qualitative indicator of resonance-driven degradation, but their relative line amplitudes need not scale one-to-one with the corresponding RDT amplitudes. In general, the skew resonances remain weaker than their normal counterparts and can be more readily mitigated; consequently, the following sections focus on the dominant normal sextupole lines and their associated RDTs.

C. Measurement of RDTs

The measurement of third-order RDTs in the Recycler Ring followed established procedures from Refs. [20,25,28], with modifications tailored to the RR. In particular, the rms momentum spread was constrained to be below 2×10^{-4} for a single batch of 81 bunches at intensities of approximately 3×10^{10} protons per bunch. These beam conditions ensured reliable synchronization of turn-by-turn BPM data and mitigated centroid decoherence. Other nominal machine and beam parameters used for the RDT measurements are summarized in Table I. The measurement procedure can be outlined as follows: (i) Excite the beam with dipole kickers and record turn-by-turn BPM data for offline analysis. (ii) Reconstruct the momentum coordinate using a least-squares fit to the lattice model, following Ref. [29]. (iii) Estimate the Twiss parameters and normalized phase-space coordinates $(\hat{w}, \hat{p}_w)$ at each BPM location for both planes $(w \in \{x, y\})$. (iv) Form the resonance basis $h_w^{\pm} = \hat{w} - i\hat{p}_w$. (v) Compute the spectrum of the resonance basis using numerical analysis of fundamental frequencies via SUSSIX [30,31]. The horizontal spectral lines (HSL) and vertical spectral lines (VSL) are indexed by j, k, l, m, with complex amplitudes HSL_{jklm} and VSL_{jklm} extracted from the spectrum (see Fig. 5 for an example). Estimate invariants I_w from the main tune peaks. (vi) Identify the spectral lines corresponding to the RDTs of interest using the equivalence tables in Ref. [25]. (vii) Determine the GFCs and RDTs at each BPM from the equivalence relations between spectral lines and RDT expansions [25].

Once the normalized phase-space coordinates are reconstructed at each BPM, the next step is to form the resonance

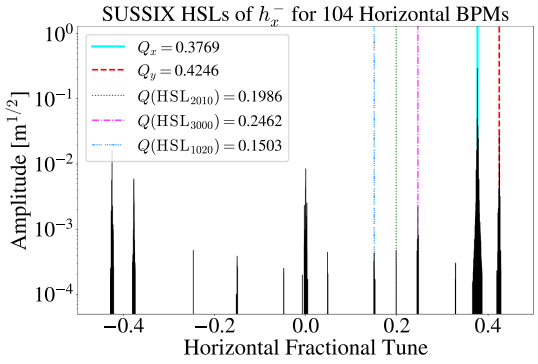


FIG. 5. Experimental measurement of spectral lines of h_x^- calculated with SUSSIX [31]. The h_x^- signal was reconstructed for the 104 horizontal BPMs. The 104 spectra for all BPMs are superimposed in this plot.

basis $h_w^{\pm}(N)$. Its spectral decomposition in the horizontal plane is given by Refs. [20,25]:

$$h_x^-(N) = \hat{x} - i\hat{p}_x = \sum_{jklm} \mathrm{HSL}_{jklm} e^{2\pi i N[(1-j+k)Q_x + (m-l)Q_y]}, \tag{5}$$

and in the vertical plane by

$$h_y^-(N) = \hat{y} - i\hat{p}_y = \sum_{jklm} \mathrm{VSL}_{jklm} e^{2\pi i N[(k-j)Q_x + (1-l+m)Q_y]}. \tag{6}$$

Here, the sums extend over the (j, k, l, m) indices. The coefficients HSL_{jklm} and VSL_{jklm} denote the complex amplitudes of the horizontal and vertical spectral lines, located at

$$Q(\mathrm{HSL}_{jklm}) = (1 - j + k)Q_x + (m - l)Q_y \tag{7}$$

and

$$Q(\mathrm{VSL}_{jklm}) = (k - j)Q_x + (1 - l + m)Q_y. \tag{8}$$

The spectral decomposition can be derived using Lie algebra methods [20,25]. In the horizontal plane this yields:

$$\begin{aligned} h_x^-(N) =& \sqrt{2I_x} e^{i(2\pi Q_x N + \psi_{x_0})} \\ & - 2i \sum_{jklm} j f_{jklm} (2I_x)^{\frac{j+k-1}{2}} (2I_y)^{\frac{l+m}{2}} \\ & \times e^{i[(1-j+k)(2\pi Q_x N + \psi_{x_0}) + (m-l)(2\pi Q_y N + \psi_{y_0})]}. \end{aligned} \tag{9}$$

The RDT measurement exploits the equivalence between Eqs. (5) and (6) and between Eq. (9) and its vertical counterpart. Therefore, the GFCs (f_{jklm}) can be related to the horizontal and vertical spectral line coefficients (HSL_{jklm} and VSL_{jklm}). Ultimately, the generating function

coefficients f_{jklm} terms can be related to resonance driving terms h_{jklm} through Eq. (4).

Figure 5 shows an example of experimental spectrum data obtained from the 104 horizontal BPMs and analyzed with SUSSIX [31]. The spectra were generated following steps 1–6 of the RDT procedure, and the results from all BPMs were superimposed to form a representative plot. The horizontal axis shows the spectral frequency (tune), while the vertical axis gives the amplitude, $|\mathrm{HSL}_{jklm}|$. Theoretical line frequencies are mapped into the $[-0.5, 0.5]$ tune domain. The dominant peak corresponds to the horizontal tune Q_x, while the second-largest peak corresponds to the vertical tune Q_y, reflecting residual transverse coupling. Several spectral lines, such as HSL_{2010}, HSL_{3000}, and HSL_{1020}, are labeled, and their amplitudes can be used to compute the associated RDTs. Other unmarked lines indicate higher-order harmonics. Notably, the amplitudes of these spectral lines are at least 2 orders of magnitude smaller than the main harmonic.

Following the spectral analysis, Fig. 6 presents an experimental measurement of the h_{3000} resonance driving term obtained by computing generalized Fourier coefficients (GFCs) and RDTs from turn-by-turn spectral data at each horizontal BPM in the Recycler Ring. The RDT amplitude $|h_{3000}|$ is extracted from the measured spectral lines using the standard normal-form formalism. Uncertainties are propagated from the spectral coefficients, tune measurements, and invariant reconstruction, including contributions from statistical fluctuations and finite measurement resolution, as described in Appendix A. Figure 6 compares the measured distribution of h_{3000} around the ring with the corresponding lattice-model prediction obtained from MAD-X PTC. The horizontal axis indicates the BPM locations, while the vertical axis shows the amplitude $|h_{3000}|$ in units of $\mathrm{m}^{-1/2}$.

The measurements reproduce the overall trend predicted by the model but exhibit reduced sensitivity to rapid local variations of the RDT. This behavior is attributed to the momentum-reconstruction algorithm described in Ref. [29], which determines the local phase-space coordinates using data from multiple neighboring BPMs (ten in the present analysis) through a least-squares procedure. As a consequence, short-wavelength BPM-to-BPM fluctuations are effectively suppressed. Additional discrepancies may arise from lattice imperfections, BPM calibration uncertainties, or residual intensity-related effects not captured in the bare-lattice calculation. Despite these differences, the overall agreement confirms that the $3Q_x = 76$ resonance is predominantly driven by systematic sextupole fields associated with the combined-function magnets.

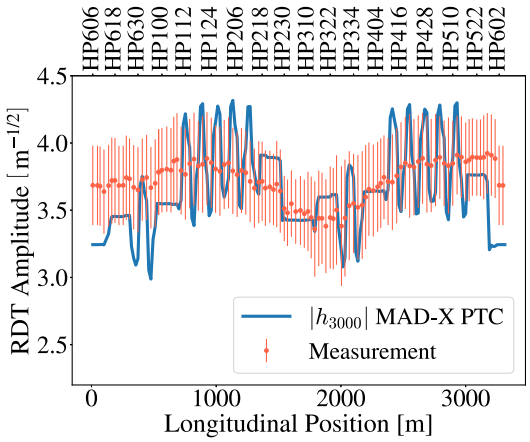


FIG. 6. Comparison between an experimental measurement of h_{3000} at all horizontal BPMs around the ring against the h_{3000} RDT calculated from MAD-X PTC. Each label in the upper axis (e.g., HP606, HP620,..., HP514) corresponds to a different horizontal BPM in the accelerator.

D. Minimization of third-order RDTs

Once the RDTs can be measured or calculated, the next step is to minimize them. The Recycler Ring is equipped with four normal sextupoles (sc220, sc222, sc319, sc321) and four skew sextupoles (ss223, ss323, ss319, ss321), commonly referred to as harmonic sextupoles, each with a magnetic length of 15.24 cm (6 in). Initial simulation studies of their effect on beam survival and emittance were reported in Ref. [4].

Canceling the h_{3000} term at a given location requires solving for the sextupole currents $I_{(i)}$ from

$$\begin{bmatrix} -|h_{3000}|\cos(\psi_{3000}) \\ -|h_{3000}|\sin(\psi_{3000}) \\ 0 \\ 0 \end{bmatrix}_{(\mathrm{Bare})} = \boldsymbol{M} \begin{bmatrix} I_{sc220} \\ I_{sc222} \\ I_{sc319} \\ I_{sc321} \end{bmatrix}, \tag{10}$$

where $\boldsymbol{M}$ is the RDT response matrix, which can be obtained from the lattice model using the definitions in Table II, explicitly from Ref. [20] or can be experimentally measured. The h_{3000} RDT is a complex quantity with a real and imaginary parts, i.e., $h_{3000} = |h_{3000}|e^{i\psi_{3000}} = |h_{3000}|\cos\psi_{3000} + i|h_{3000}|\sin\psi_{3000}$.

Canceling the one-turn h_{3000} RDT at a single location does not necessarily yield the best overall compensation. Figure 7 illustrates the behavior of the other relevant RDTs when h_{3000} is canceled at the starting point $s = 0$ for MAD-X PTC lattice-model calculation. In this case, the amplitude of h_{1020} increases significantly compared to Fig. 4; for example, between BPMs HP408 and HP514 the peak value nearly triples. Thus, compensating the $3Q_x = 76$ resonance inevitably worsens the $Q_x + 2Q_y = 74$ line, underscoring the need for care when attempting simultaneous compensation of multiple resonances.

Figure 7 illustrates a lattice-model approach to RDT cancellation. Experimentally, the response matrix $\boldsymbol{M}$ is obtained by measuring h_{3000} as a function of the compensation sextupole currents and isolating the sextupole contribution from the bare-machine value, i.e., $h_{3000}^{(\mathrm{sext})} = h_{3000} - h_{3000}^{(\mathrm{Bare})}$. Figure 8 shows an example scan for the

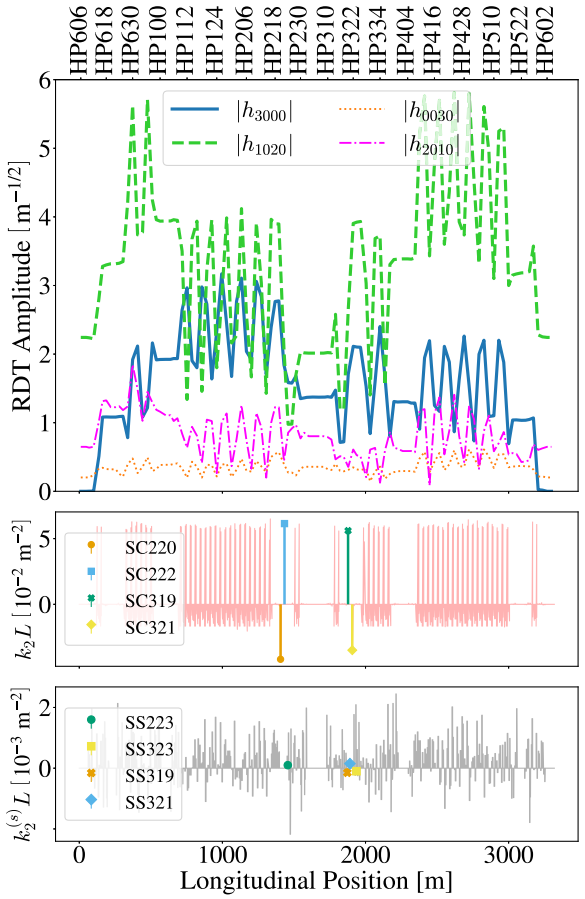


FIG. 7. Lattice-model calculation of the relevant third-order RDTs, i.e., h_{3000}, h_{1020}, h_{0030}, and h_{2010}, around the ring from an arbitrary starting point as calculated from the lattice model using the MAD-X PTC module with compensation for $h_{3000}(s=0)$. Each label in the upper axis (e.g., HP606, HP620, ... , HP514) corresponds to a different horizontal BPM in the accelerator.

sc222 sextupole. Within the shaded region, the real and imaginary parts of h_{3000} vary linearly with sextupole current, and the response matrix coefficients are extracted from the slopes of the fitted lines. This procedure was applied to h_{3000} and h_{1020} using the normal sextupoles $(I_{\mathrm{sc220}}, I_{\mathrm{sc222}}, I_{\mathrm{sc319}}, I_{\mathrm{sc321}})$ and to h_{0030} and h_{2010} using the skew sextupoles $(I_{\mathrm{ss223}}, I_{\mathrm{ss323}}, I_{\mathrm{ss319}}, I_{\mathrm{ss321}})$. As expected, the normal sextupoles do not produce measurable effects in the skew RDTs, and vice versa.

After measuring the bare-machine RDTs, scanning the sextupole currents, and constructing the response matrices, the compensation currents solving Eq. (10) were calculated at each BPM. Equation (10) can be generalized to include additional RDTs on the left-hand side or more compensation elements on the right. Since $\boldsymbol{M}$ is not necessarily square, the system is typically solved in a least-squares sense, with the option of including user-defined constraints. In practice, not all RDTs can be accessed experimentally, as some do not appear as clear spectral lines due to BPM resolution, electronic noise, or unfavorable beam

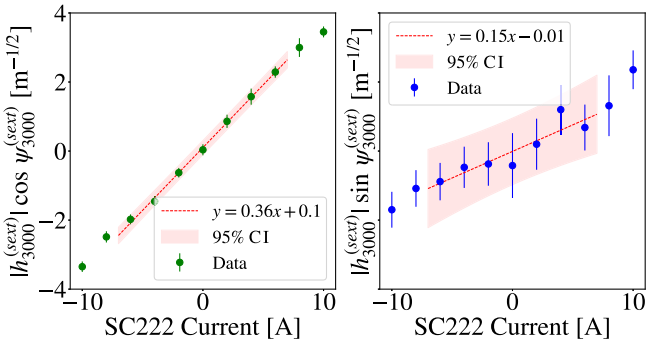


FIG. 8. Experimental measurement of the real and imaginary parts of h_{3000} as a function of current fed to compensation sextupole SC222 with the linear regression and its 95% confidence interval (CI). Measurement is shown for the arbitrary BPM R:HP126.

conditions such as rapid decoherence, large emittance, or weak oscillation signals at low intensity. In addition, the Recycler Ring provides only eight harmonic sextupoles (four normal and four skew) as correction elements, and in some cases the required solutions for the sextupole currents exceed the hardware limits of these magnets.

This procedure yields an array of predicted compensation currents, one from each BPM. Figure 9 shows an example for minimizing the h_{3000} term: each point represents the local current predicted to minimize h_{3000} at that BPM. Because the sextupoles can only be set to a single value, these predictions are averaged to obtain a global current that reduces the RDT across the ring, though not necessarily canceling it completely, consistent with the conclusions of Refs. [21,22]. Once this setting is established, the next step is to verify experimentally that the resonance strength is reduced.

E. Experimental verification of compensation

The experimental verification of the compensation currents was carried out using static tune scans and dynamic

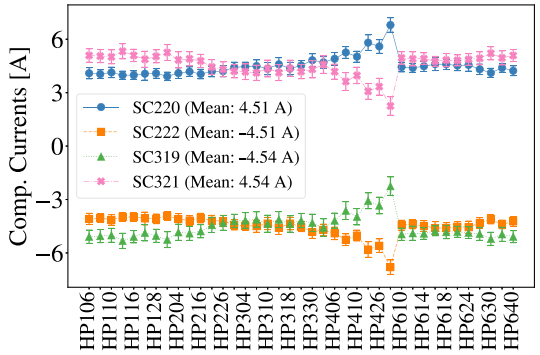


FIG. 9. Experimental compensation currents calculated for every BPM that minimizes the h_{3000} RDT at that particular location.

loss maps. In the static scan method, the tunes were set to fixed values while monitoring the beam survival ratio (BSR) and beam size growth (BSG) over a time interval of about 0.8 s, corresponding to roughly 72,800 turns. The BSR was obtained from beam intensity measurements using the dc current transformer, while the BSG was determined with the ion profile monitor (IPM) system [24]. In this case, the beam size is defined as the rms σ extracted from a Gaussian fit to the measured IPM profiles.

Figure 10 shows a static tune scan comparing experimental data (beam survival ratio I_f/I_0 and maximum beam size growth $\sigma_{\max}/\sigma_0$) with Xsuite tracking simulations [32]. The experiment was performed at an intensity of 0.5×10^{10} protons per bunch, for which the estimated rms space-charge tune spread is $\Delta Q_{\mathrm{SC}} \sim 7 \times 10^{-4}$. Using the nominal rms momentum spread $\sigma_{\delta/p} = 4 \times 10^{-4}$ (Ref. [4]) and the natural chromaticities $\xi_x = -7$ and $\xi_y = -6$, the corresponding rms chromatic tune spread is $\Delta Q_{\mathrm{chrom}} \sim 3 \times 10^{-3}$. Since the space-charge tune spread is smaller than the chromatic tune spread, nonlinear lattice effects are expected to be more relevant than direct space charge, justifying the neglect of space charge in the Xsuite simulations. Furthermore, the space-charge tune shift is significantly smaller than the stop band width of the third-order resonance, which is of order 0.02.

The Recycler lattice was imported from MAD-X through the Xsuite interface, and particles were tracked for 72,800 turns with the Recycler Ring's elliptical aperture. Combined-function magnets were modeled as two thin multipoles (one normal and one skew), a gradient magnet, and two additional multipoles, with baseline coefficients taken from magnet measurements to account for field errors and shims. Chromaticity was set to its natural value by switching off the chromatic sextupoles, consistent with the experimental conditions. Tunes were varied using the tune trombone quadrupoles by introducing local phase advances. The initial beam was generated as a matched Gaussian distribution with normalized 95% transverse emittance of 15 π mm mrad and longitudinal emittance of 0.07 eV s. No explicit truncation was applied to the distribution; in practice, the finite precision of the sampling ensures negligible population at large amplitudes. Beam sizes and rms emittances were computed from the second moments of the surviving particle distribution on a turn-by-turn basis. Table III summarizes the simulation parameters.

TABLE III. Base parameters for Xsuite simulations.

Parameter	Value	Unit
Number of particles	100,000	
Number of turns	72,800	
Momentum	8.835	GeV/c
rf voltage	80	kV
Harmonic number	588	
Horizontal chromaticity	−5.73	
Vertical chromaticity	−7.81	
95% normalized emittance	15	π mm mrad
Longitudinal bunch length	0.6	m
95% longitudinal emittance	0.07	eV s

Figure 10 shows the resonance stop band associated with the $3Q_x$ line. When the working point coincides with the resonance condition, essentially no beam survival is observed. The simulated stop band width, approximately 0.02 in tune units, is in good agreement with the experimental data, indicating that the model captures the dominant sextupole components around the ring, even if not in perfect detail. For tune values below the resonance, the experimental data exhibit slight deviations from the model, reflecting the fact that the Recycler Ring is not optimized for operation in this tune region.

Figure 11 presents an analogous comparison with compensation applied. In the simulations, the optimal

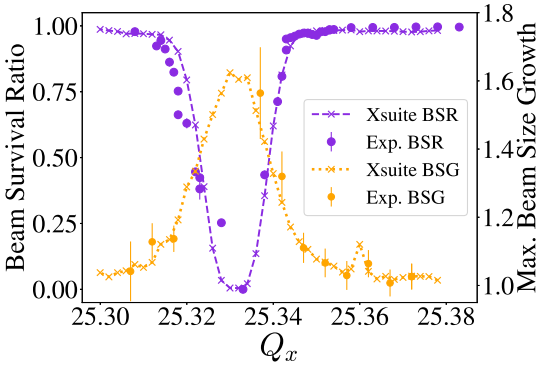


FIG. 10. Static tune scan for the bare machine with comparisons between experimental data and Xsuite tracking simulations (no space charge) at a low intensity of 0.5×10^{10} particles per bunch for 72,800 turns. The maximum beam size growth (BSG) from the simulations and the experimental IPM measurements are also plotted on the secondary axis.

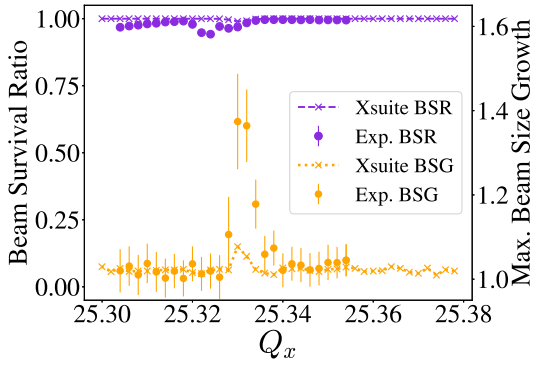


FIG. 11. Static tune scan with compensated $3Q_x$ for the bare machine with comparisons between experimental data and Xsuite simulations at a low intensity of 0.5×10^{10} particles per bunch. Left vertical axis corresponds to beam survival ratio (BSR) and right one to maximum beam size growth (BSG). The experimental BSG was measured with the IPM system.

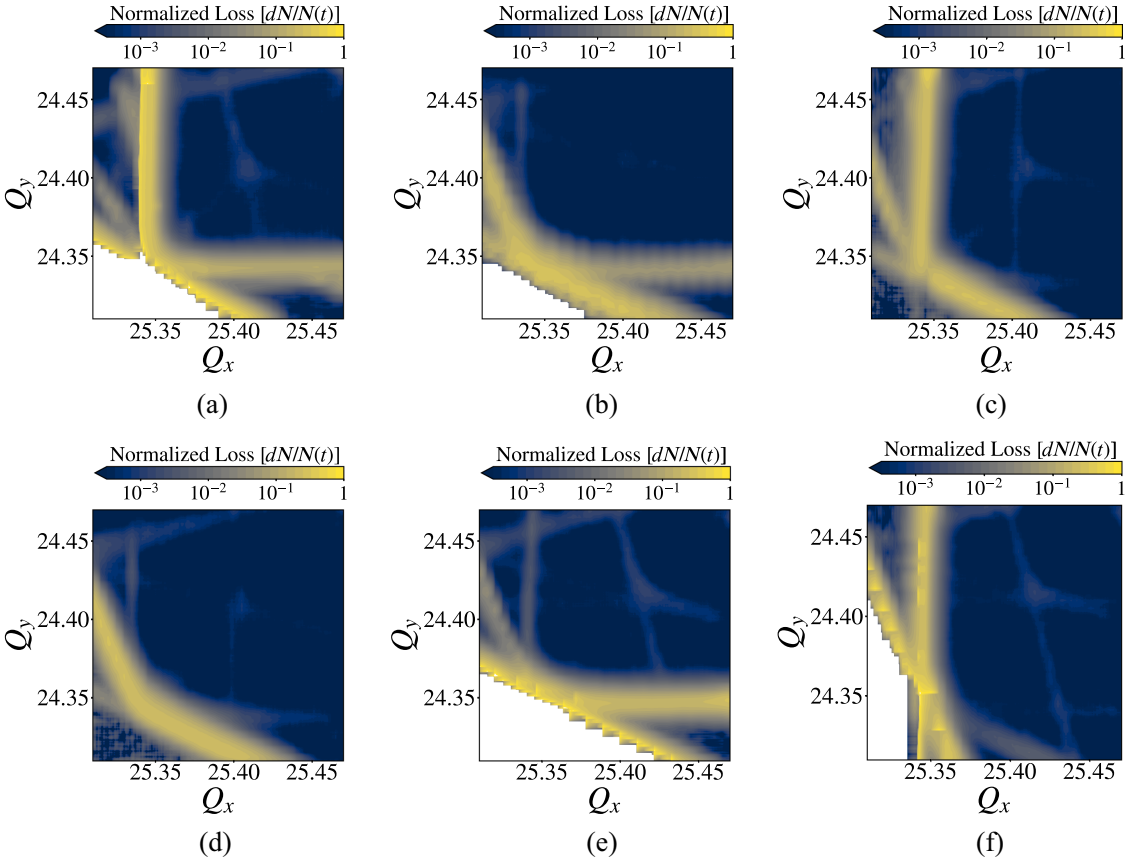


FIG. 12. Experimental dynamic loss maps for several configurations of compensation sextupoles: (a) bare machine, (b) $3Q_x$ compensation, (c) $3Q_y$ compensation, (d) $3Q_x$ and $3Q_y$ compensation, (e) $3Q_x$ and $2Q_x + Q_y$ compensation, and (f) $3Q_y$ and $Q_x + 2Q_y$ compensation.

K_2L strengths of the compensation sextupoles were computed by minimizing the h_{3000} resonance driving term around the ring, and the beam was tracked for 72,800 turns with intensity and beam size recorded every 100 turns. The resulting theoretical K_2L values can converted to sextupole currents using magnet calibration data. Experimentally, the compensation currents were obtained using the response matrix method and further refined through a Nelder-Mead optimization based on measured beam losses. In both simulation and experiment, compensation improves the beam survival ratio near the $3Q_x$ resonance by reducing losses at the resonance location. The simulations, however, systematically predict smaller beam size growth than observed experimentally, which is attributed to unmodeled effects such as residual space charge and measurement uncertainties in the IPM system.

To quantify the level of agreement between the optimal sextupole settings obtained from simulation and experiment, we compare the resulting compensation currents for different mitigation scenarios. For the mitigation of individual resonance lines, the optimal currents differ by no more than approximately 10% for normal sextupole resonances and by no more than approximately 50% for skew resonances. The absolute currents required to mitigate normal sextupole resonances are typically about 4 times larger than those required for skew resonances. For the simultaneous mitigation of two resonance lines, theoretical K_2L and $K_2^{(s)}L$ values were computed to minimize both RDTs around the ring, while experimentally the optimal currents were obtained from the RDT response matrices with additional multiobjective optimization. In these multiline cases, the optimal currents from theory and experiment differ by up to approximately 120%, while generally predicting the same current polarity. Such differences are consistent with unmodeled nonlinear lattice effects, including unaccounted normal and skew sextupole components, as well as possible tilts or rolls of the sextupole and skew sextupole correctors and other lattice elements. Overall, these results indicate that simulation and experiment identify consistent compensation patterns and jointly validate the effectiveness of RDT-based compensation in mitigating third-order resonance effects in the Recycler Ring.

Dynamic loss maps were also employed to verify the effectiveness of compensation. Figure 12 shows examples for different sextupole configurations. The bare machine case, with no compensation applied, is shown in Fig. 12(a), while Figs. 12(b) and 12(c) illustrate compensation targeted at a single resonance line. For the $3Q_x$ resonance, the four

normal sextupoles were set to the currents calculated with the experimental RDT response matrix method. A comparison between Figs. 12(a) and 12(b) reveals that compensation reduces normalized losses at the $3Q_x$ line by nearly 2 orders of magnitude. A similar effect is observed for $3Q_y$ compensation in Fig. 12(c).

Figures 12(d)–12(f) present optimal sextupole configurations designed to compensate multiple resonances simultaneously. However, compensating one or more lines can inadvertently amplify others, as previously shown in Fig. 7. For example, Fig. 12(f) demonstrates that compensating $3Q_y$ and $Q_x + 2Q_y$ strengthens the $2Q_x + Q_y$ resonance. Such trade-offs become more pronounced when attempting to cancel more than two lines, since the required sextupole currents increase and can exceed hardware limits. This occurs when compensating both normal sextupole lines, $3Q_x$ and $Q_x + 2Q_y$, where the predicted currents surpass the supply range.

Overall, the loss maps in Fig. 12 illustrate how RDT minimization can be used to suppress resonance-driven losses across a broad region of tune space, thereby enabling larger tune spreads for high-intensity operation in the PIP-II era.

III. CHARACTERIZATION OF COMPENSATION AT HIGH INTENSITIES

A. Space charge tune shift

The previous section demonstrated how resonance lines can be mapped with low-intensity beams to verify mitigation strategies. At higher intensities, however, the incoherent space-charge tune spread must be taken into account, as illustrated in Fig. 2. Figure 13 shows slices of dynamic loss maps at different intensities for a fixed vertical tune. Resonance crossing with space charge is a complex process [14,33–35]: depending on the crossing speed, particles may either lock to a resonance or scatter off it. The measurements in Fig. 13 reveal that essentially no beam survives when crossing the $3Q_x = 76$ resonance, indicating that most particles are eventually captured. The top slice corresponds to an intensity of 2 booster turns (BTs), about 0.6×10^{10} particles per bunch (ppb), while the bottom slice corresponds to 17 BTs, or roughly 6.0×10^{10} ppb, close to the Booster single-batch maximum. These measurements were performed with bunched beam at nonzero chromaticity under conditions close to those listed in Table III. The corresponding incoherent space-charge tune shifts, calculated from measured emittances using the formalism of Ref. [36], are shown in Fig. 14. The error analysis for the tune spread is explained in Appendix B. Notably, the incoming booster emittance increases with intensity, transitioning from an approximately constant regime at low intensity to a roughly linear dependence at higher intensity, consistent with operational brightness limitations observed in high-intensity injectors [37]. The

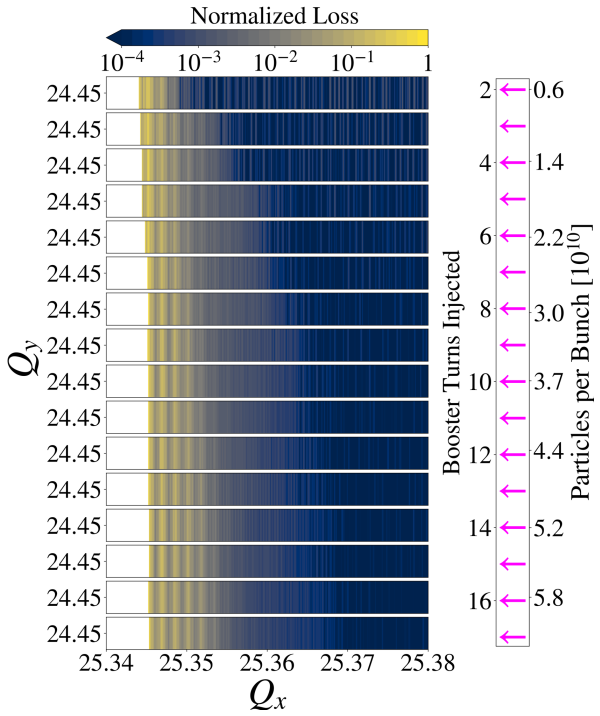


FIG. 13. Experimental dynamic loss strips at a fixed vertical set tune of $Q_y = 24.45$ and on a range from $Q_x = 25.39$ to $Q_x = 25.32$ for different intensities.

intermediate intensity range represents a transient region between these two behaviors rather than a distinct exponential growth.

As the intensity increases, beam losses occur progressively earlier in the tune ramp. The tune distance between the onset of losses and total beam loss (marked by the start of the white region) grows with intensity and saturates at about 0.02 beyond 4.0×10^{10} ppb. This metric is also plotted in Fig. 14, where it scales well with the calculated space-charge tune spread.

This behavior can be interpreted, following Ref. [14], as a two-stage process: scattering of particles off the resonance driven by space charge and synchrotron motion when sufficiently far from the stop band, followed by adiabatic trapping of particles as the resonance is approached. For example, for the 5.8×10^{10} ppb case, losses begin near $Q_x \approx 25.37$ and rise gradually until $Q_x \approx 25.355$, consistent with scattering effects, while the sharp increase in loss rate between $Q_x \approx 25.355$ and 25.345 reflects adiabatic locking of particles into the resonance.

The maximum tune spread observed in Fig. 14 is about 0.02, corresponding to only one-fifth of the projected value for PIP-II. These measurements were performed with a single batch and without slip stacking. Under PIP-II conditions, with slip stacking and the smaller emittance expected from the booster, tune spreads in the recycler of up to 0.09 are anticipated. At present, however, the tune spreads remain modest and are not yet a limiting factor for operation.

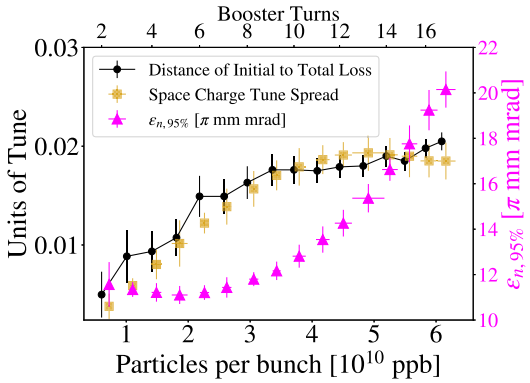


FIG. 14. Space-charge tune spread (gold squares, left axis) calculated from horizontal emittances (fuchsia triangles, right axis) measured with multiwire data from first-turn abort beam. The distance between initial and total beam loss (black circles) is plotted on the left axis for reference.

B. Static tune scans

Gaussian and q-Gaussian fits provide a framework to analyze static tune scans at higher intensities for bunched beams with sextupole compensation. In particular, q-Gaussian distributions quantify the degree of transverse tail population [38–40]. The case $q = 1$ corresponds to a Gaussian distribution, $q > 1$ indicates heavy tails, $q < 1$ underpopulated tails, and $q = 2$ recovers the Cauchy-Lorentzian. Figures 15–17 present the average q values at each tune and intensity from IPM data, where only fits passing a chi-square goodness-of-fit test at the 95% confidence level are reported. These figures also show the beam survival ratio and the evolution of the horizontal normalized emittance versus turns, with color encoding turn number: blue for early turns near injection and yellow for later times in the cycle.

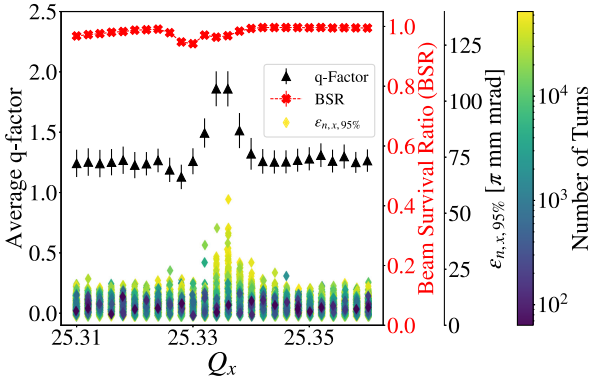


FIG. 15. Experimental static tune scan with beam survival ratio (BSR), average q-factor for the q-Gaussian fits, and normalized emittance at an equivalent intensity of 2 booster turns or approximately 0.5×10^{10} ppb. The horizontal set tune was varied from 25.37 to 25.31 while the vertical set tune was fixed at 24.44. IPM data were collected every 64 turns over 65,000 real turns in the machine.

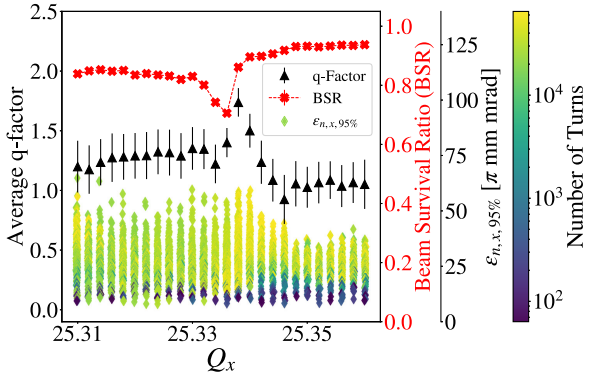


FIG. 16. Experimental static tune scan with beam survival ratio (BSR), average q-factor for the q-Gaussian fits, and normalized emittance at an equivalent intensity of 8 booster turns or approximately 3.0×10^{10} ppb. The horizontal set tune was varied from 25.37 to 25.31 while the vertical set tune was fixed at 24.44. IPM data were collected every 64 turns over 65,000 real turns in the machine.

Beam dynamics near third-order resonances in bunched high-intensity beams can be understood by distinguishing between incoherent single-particle dynamics and the collective response of the space-charge-dominated core. In the incoherent picture, particles may be trapped into or scattered by resonance islands whose effective location is modulated by synchrotron motion [14,41,42]. When the space-charge tune spread is comparable to, or smaller than, externally imposed tune spreads (e.g., from chromaticity), resonance interaction can be interpreted predominantly in terms of incoherent single-particle dynamics across the tune distribution. This is the case for the low-intensity conditions in Fig. 15, where $\Delta Q_{\mathrm{SC}} \sim 7 \times 10^{-4}$ is smaller than $\Delta Q_{\mathrm{chrom}} \sim 3 \times 10^{-3}$.

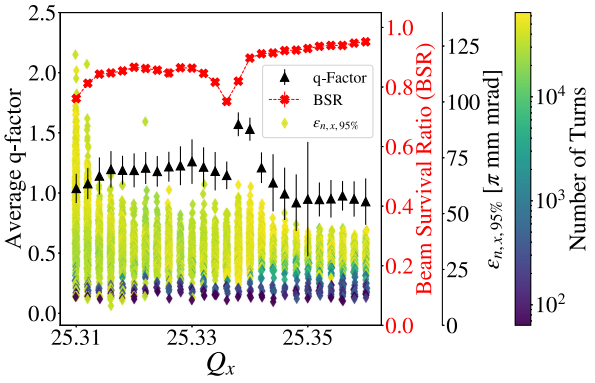


FIG. 17. Experimental static tune scan with beam survival ratio (BSR), average q-factor for the q-Gaussian fits, and normalized emittance at an equivalent intensity of 14 booster turns or approximately 4.5×10^{10} ppb. The horizontal set tune was varied from 25.37 to 25.31 while the vertical set tune was fixed at 24.44. IPM data were collected every 64 turns over 65,000 real turns in the machine.

In contrast, for the high-intensity conditions shown in Figs. 16 and 17, the space-charge tune spread becomes the dominant contribution to the overall tune footprint ($\Delta Q_{\mathrm{SC}} \sim 1.8 \times 10^{-2} > \Delta Q_{\mathrm{chrom}} \sim 3 \times 10^{-3}$). In this regime, the resonant response of the beam core is expected to occur around the collective (coherent) frequency with a finite stop band width, as discussed in Refs. [43–45]. Emittance growth and losses are then driven primarily by incoherent particles whose tunes satisfy the resonance condition away from the coherent/core frequency, i.e., outside the collective core stop band, through trapping and scattering in space-charge-modified resonance islands modulated by synchrotron motion. As emittance growth reduces the space charge tune shift, the system may transition from the space-charge-dominated regime back to a mixed or weakly space-charge-dominated regime, where lattice nonlinearities dominate the dynamics.

At low intensity (Fig. 15), the beam survival ratio improves with $3Q_x$ compensation, yet residual losses appear through a rise in the q factor. Near $Q_x = 25.335$, the survival ratio decreases slightly while both the normalized emittance and average q increase. After tens of thousands of turns, the emittance grows, showing that residual resonance-driving terms still feed the $3Q_x$ line. The concurrent increase in q indicates enhanced tail population: low-amplitude particles diffuse outward, increasing emittance, while high-amplitude particles become trapped in resonance islands and are eventually lost at the aperture. The average q value is slightly above unity ($q \approx 1.2$), indicating that raw IPM profiles deviate from a Gaussian. This effect is absent in Figs. 16 and 17, where q values before the resonance remain close to 1.0. It should also be noted that the IPM system is optimized for higher intensities [24].

For static tune scans at higher intensities, such as 3.0×10^{10} ppb in Fig. 16 and 4.5×10^{10} ppb in Fig. 17, space-charge effects dominate the beam dynamics. The two cases exhibit similar behavior because the space-charge tune shift saturates near $\Delta Q_{\mathrm{SC}} \simeq 0.02$, as previously discussed for Fig. 14, primarily due to emittance growth out of the booster. In this regime, the maximum emittance growth is observed to shift to the right of the nominal third-order resonance, consistent with the experimental findings of Ref. [14]. Furthermore, the maximum q-factor increase also shifts to the right. As the horizontal tune approaches the resonance, the emittance increases toward the machine acceptance within $\sim 20,000$ turns, leading to a reduction of the beam survival ratio below unity.

Following the interpretation of Ref. [14], this emittance growth arises from the combined effect of strong space charge and synchrotron motion, which induces a periodic crossing of resonances. Low-amplitude particles belonging to the beam core are repeatedly scattered across the space-charge-induced resonance islands; although the core responds collectively around the coherent frequency [43–45], individual core particles undergo resonant diffusion to larger amplitudes, driving emittance growth, while losses occur when high-amplitude particles become trapped in resonance islands and are transported into the aperture. The q-factor peaks near $Q_x \approx 25.34$, shifted to the right with respect to the low-intensity case at $Q_x \approx 25.33$, reflecting enhanced transverse tail population prior to significant particle loss. Losses peak where the q-factor rises and the emittance has already approached the machine acceptance. To the left of the resonance, the emittance grows more rapidly, consistent with interaction with the coupled third-order line $2Q_x + Q_y = 75$ and with the recycler not being optimized for stable operation in this tune region.

The minimization of RDTs around the ring provides an effective strategy to mitigate third-order resonance losses, even at intensities relevant for PIP-II operation. Without compensation, essentially no beam survives across the $3Q_x$ line (Fig. 10), whereas RDT minimization significantly reduces losses. In practice, this scheme decreases the width of the resonance islands and the associated diffusion driven by third-order fields and space charge, thereby lowering the probability of particle trapping and subsequent loss. While the results presented focus on the $3Q_x = 76$ resonance, the conclusions extend to the other third-order lines in the Recycler Ring.

C. Conclusions and outlook

This paper has presented the implementation of resonance driving term (RDT) minimization to mitigate losses from third-order resonances in the Fermilab Recycler Ring. We first outlined the theoretical framework for minimizing third-order RDTs and then developed an experimental scheme validated through static tune scans and dynamic loss maps. The method was further tested at higher intensities using q-Gaussian beam characterization. Our work extends literature on high-intensities bunched beams by characterizing third-order resonances under conditions where RDT minimization methods are applied. Although present operational losses are not dominated by space charge, the compensation scheme established here will become increasingly important in the PIP-II era. To strengthen this approach, an additional pair of sextupoles has recently been installed in the recycler (commissioning pending), enabling future studies of multiobjective minimization with a larger set of compensation elements. Further simulation work including space charge is also required to better understand tail-population mechanisms and the emergence of q-Gaussian beam profiles.

ACKNOWLEDGMENTS

This manuscript has been authored by Fermi Forward Discovery Group, LLC (FFDG) under Contract No. 89243024CSC000002 with the U.S. Department of Energy, Office of Science, Office of High Energy Physics. We would like to acknowledge the Accelerator Science and

Engineering Traineeship (ASET) program at Michigan State University. The ASET program is partially supported by the U.S. Department of Energy, Office of Science, High Energy Physics under Cooperative Agreement Award No. DE-SC0018362 and Michigan State University. C. G.-O. and R. A. would also like to acknowledge the whole MI/RR department at Fermilab who supported this research.

DATA AVAILABILITY

The data that support the findings of this article are openly available [46].

APPENDIX A: ERROR BARS IN RDT AMPLITUDE MEASUREMENT

The resonance driving term (RDT) amplitude $|h_{jklm}|$ is inferred from the generating function coefficient f_{jklm} and the machine tunes through

$$\begin{aligned}|h_{jklm}| &= |f_{jklm}||1 - e^{2\pi i[(j-k)Q_x+(l-m)Q_y]}| \\ &= 2|f_{jklm}||\sin(\pi Q)|,\end{aligned} \tag{A1}$$

where we introduced the resonance phase combination

$$Q = (j-k)Q_x + (l-m)Q_y. \tag{A2}$$

It is well known that the RDT expansion becomes invalid when Q approaches an integer value, i.e., in the vicinity of a resonance line, where the underlying assumptions of the approximation break down [25].

This expression shows that the measured amplitude is the product of the amplitude of the generating function coefficient $|f_{jklm}|$ and a tune-dependent geometric factor depending on the j, k, l and m indices of the perturbation.

Assuming that $|f_{jklm}|$, Q_x, and Q_y are measured independently, the variance of the RDT amplitude follows from standard error propagation:

$$\begin{aligned}\sigma^2_{|h_{jklm}|} = {} & 4\sigma^2_{|f_{jklm}|}\sin^2(\pi Q) + (2\pi|f_{jklm}|\cos(\pi Q))^2 \\ & \times \left[(j-k)^2\sigma^2_{Q_x} + (l-m)^2\sigma^2_{Q_y}\right].\end{aligned} \tag{A3}$$

The first term represents the contribution from the statistical and measurement uncertainty of the spectral coefficient $|f_{jklm}|$, while the second term quantifies how tune uncertainties propagate through the factor $\sin(\pi Q)$ and therefore modulate the inferred $|h_{jklm}|$.

Dividing by $|h_{jklm}|^2$ yields a compact relative-error form,

$$\begin{aligned}\left(\frac{\sigma_{|h_{jklm}|}}{|h_{jklm}|}\right)^2 \simeq {} & \left(\frac{\sigma_{|f_{jklm}|}}{|f_{jklm}|}\right)^2 \\ & + \left[\pi\cot(\pi Q)\right]^2\left[(j-k)^2\sigma^2_{Q_x} + (l-m)^2\sigma^2_{Q_y}\right],\end{aligned} \tag{A4}$$

which makes explicit that tune errors become increasingly important when $|\sin(\pi Q)|$ is small (i.e., close to integer values of Q), where the $\cot(\pi Q)$ factor enhances the sensitivity.

In practice, the coefficient $|f_{jklm}|$ is obtained from the measured spectral-line amplitude $|\mathrm{HSL}_{jklm}|$ after normalizing by the invariants I_x and I_y according to

$$|\mathrm{HSL}_{jklm}| = 2\,j\,(2I_x)^{\frac{j+k-1}{2}}(2I_y)^{\frac{l+m}{2}}|f_{jklm}|. \tag{A5}$$

Therefore, the uncertainty on $|f_{jklm}|$ inherits contributions from the measurement of the spectral line itself and from the invariant measurements (I_x, I_y). The invariants are estimated from the main tune peak of the resonance basis spectrum. Propagating errors through the above normalization gives

$$\begin{aligned}\left(\frac{\sigma_{|f_{jklm}|}}{|f_{jklm}|}\right)^2 \simeq {} & \left(\frac{\sigma_{|HSL_{jklm}|}}{|HSL_{jklm}|}\right)^2 \\ & + \left(\frac{j+k-1}{2}\right)^2\left(\frac{\sigma_{I_x}}{I_x}\right)^2 + \left(\frac{l+m}{2}\right)^2\left(\frac{\sigma_{I_y}}{I_y}\right)^2.\end{aligned} \tag{A6}$$

Substituting this result into the relative-error expression for $|h_{jklm}|$ yields a complete uncertainty budget that separates (i) the statistical uncertainty of the measured harmonic line, (ii) the combined statistical and measurement-resolution contributions associated with the invariant determination, and (iii) the contribution from tune measurement uncertainty through the $\cot(\pi Q)$ sensitivity factor. In practice, the dominant sources of uncertainty in the RDT measurement arise from the statistical uncertainty in the spectral-line amplitude and phase extraction, together with finite measurement precision in the invariant reconstruction.

APPENDIX B: ERROR BARS IN SPACE CHARGE TUNE SPREAD

The incoherent space-charge tune spread is estimated using the formalism in Ref. [36]:

$$\Delta Q_{\mathrm{sc}} = \frac{-3Nr_0RS}{4\sigma_z M\beta\gamma^2\varepsilon_{N,95\%}}, \tag{B1}$$

where N is the total beam intensity, r_0 the classical particle radius, R the machine radius, S the longitudinal form factor, σ_z the rms bunch length, M the number of bunches, β and γ the relativistic factors, and $\varepsilon_{N,95\%}$ the normalized 95% transverse emittance.

To estimate the uncertainty on ΔQ_{sc}, we propagate the measurement errors of the quantities entering the above expression using standard first-order error propagation. The uncertainties associated with β, γ, and M are neglected, as these quantities are fixed by the beam energy and the rf configuration and are therefore known with higher precision than the emittance and bunch-length measurements.

Assuming that the individual measurements are uncorrelated, the relative uncertainty on the space-charge tune spread can be written as

$$\left(\frac{\sigma_{\Delta Q_{\mathrm{sc}}}}{|\Delta Q_{\mathrm{sc}}|}\right)^2 \simeq \left(\frac{\sigma_N}{N}\right)^2 + \left(\frac{\sigma_S}{S}\right)^2 + \left(\frac{\sigma_{\sigma_z}}{\sigma_z}\right)^2 + \left(\frac{\sigma_{\varepsilon_{N,95\%}}}{\varepsilon_{N,95\%}}\right)^2. \tag{B2}$$

In this analysis, the dominant sources of uncertainty arise from the determination of the normalized transverse emittance $\varepsilon_{N,95\%}$ and the rms bunch length σ_z, both of which are obtained from fits to multiwire and longitudinal diagnostic data, respectively. The bunch form factor S is evaluated assuming a Gaussian longitudinal charge distribution, and its uncertainty reflects the sensitivity to this assumption. The beam intensity N is measured using calibrated intensity diagnostics; its relative uncertainty is therefore small compared to the contributions from the emittance and bunch-length measurements and is treated as subdominant in the total error budget.

[1] G. Jackson, The Fermilab recycler ring technical design report. Revision 1.2, Technical Report No. FNAL-TM-1991ON: DE97051388; BR: KAHEP, Fermilab, 1996, 10.2172/16029.

[2] P. Adamson *et al.*, The NuMI neutrino beam, Nucl. Instrum. Methods Phys. Res., Sect. A **806**, 279 (2016).

[3] R. Ainsworth, P. Adamson, B. C. Brown, D. Capista, K. Hazelwood, I. Kourbanis, D. K. Morris, M. Xiao, and M.-J. Yang, High intensity operation using proton stacking in the Fermilab Recycler to deliver 700 kW of 120 GeV proton beam, Phys. Rev. Accel. Beams **23**, 121002 (2020).

[4] R. Ainsworth, P. Adamson, J. Amundson, I. Kourbanis, Q. Lu, and E. Stern, High intensity space charge effects on slip stacked beam in the Fermilab recycler, Phys. Rev. Accel. Beams **22**, 020404 (2019).

[5] R. Ainsworth, P. Adamson, D. Capista, N. Chelidze, C. Gonzalez-Ortiz, K. Hazelwood, I. Kourbanis, O. Mohsen, D. Morris, M. Murphy, M. Wren, and M. Xiao, Improvements to the recycler/main injector to deliver 850 kW+, in *Proceedings of the 5th International Particle Accelerator Conference (NAPAC2022), Albuquerque, NM, USA* (JACoW, Geneva, Switzerland, 2022), 10.18429/JACoW-NAPAC2022-WEYE3.

[6] M. Ball *et al.*, The PIP-II conceptual design report, Technical Report No. FERMILAB-TM-2649-AD-APC1516858, Fermilab, 2017, 10.2172/1346823.

[7] F. Asvesta, PySCRDT, https://github.com/fasvesta/tune-spread/tree/master (2019).

[8] F. Asvesta and H. Bartosik, Resonance driving terms from space charge potential, Technical Report No. CERN-ACC-NOTE-2019-0046, 2019, https://cds.cern.ch/record/2696190/files/CERN-ACC-NOTE-2019-0046.pdf.

[9] F. Asvesta, S. Albright, F. Antoniou, H. Bartosik, C. Bracco, G. P. Di Giovanni, E. Maclean, B. Mikulec, T. Prebibaj, and E. Renner, Resonance compensation for high intensity and high brightness beams in the CERN PSB, in *Proceedings of the 64th ICFA ABDW on High-Intensity and High-Brightness Hadron Beams (HB2021), Batavia, IL, USA* (JACoW, Geneva, Switzerland, 2022), pp. 40–45, 10.18429/JACoW-HB2021-MOP06.

[10] F. Asvesta, H. Bartosik, S. Gilardoni, A. Huschauer, S. Machida, Y. Papaphilippou, and R. Wasef, Identification and characterization of high order incoherent space charge driven structure resonances in the CERN Proton Synchrotron, Phys. Rev. Accel. Beams **23**, 091001 (2020).

[11] E. H. Maclean, R. Tomás, F. S. Carlier, M. S. Camillocci, J. W. Dilly, J. Coello de Portugal, E. Fol, K. Fuchsberger, A. Garcia-Tabares Valdivieso, M. Giovannozzi, M. Hofer, L. Malina, T. H. B. Persson, P. K. Skowronski, and A. Wegscheider, New approach to LHC optics commissioning for the nonlinear era, Phys. Rev. Accel. Beams **22**, 061004 (2019).

[12] G. Franchetti, I. Hofmann, M. Giovannozzi, M. Martini, and E. Metral, Space charge and octupole driven resonance trapping observed at the CERN Proton Synchrotron, Phys. Rev. ST Accel. Beams **6**, 124201 (2003).

[13] T. Yasui, S. Igarashi, Y. Sato, and T. Koseki, Beam optics for the compensation of third-order structure resonances, Prog. Theor. Exp. Phys. **2022**, 013G01 (2022).

[14] G. Franchetti, O. Chorniy, I. Hofmann, W. Bayer, F. Becker, P. Forck, T. Giacomini, M. Kirk, T. Mohite, C. Omet, A. Parfenova, and P. Schütt, Experiment on space charge driven nonlinear resonance crossing in an ion synchrotron, Phys. Rev. ST Accel. Beams **13**, 114203 (2010).

[15] G. Franchetti, S. Gilardoni, A. Huschauer, F. Schmidt, and R. Wasef, Space charge effects on the third order coupled resonance, Phys. Rev. Accel. Beams **20**, 081006 (2017).

[16] I. Hofmann, A. Oeftiger, and O. Boine-Frankenheim, Self-consistent long-term dynamics of space charge driven resonances in 2D and 3D, Phys. Rev. Accel. Beams **24**, 024201 (2021).

[17] A. Oeftiger, O. Boine-Frankenheim, V. Chetvertkova, V. Kornilov, D. Rabusov, and S. Sorge, Simulation study of the space charge limit in heavy-ion synchrotrons, Phys. Rev. Accel. Beams **25**, 054402 (2022).

[18] R. Tomás, M. Bai, R. Calaga, W. Fischer, A. Franchi, and G. Rumolo, Measurement of global and local resonance terms, Phys. Rev. ST Accel. Beams **8**, 024001 (2005).

[19] A. Franchi, L. Farvacque, F. Ewald, G. Le Bec, and K. B. Scheidt, First simultaneous measurement of sextupolar and octupolar resonance driving terms in a circular accelerator from turn-by-turn beam position monitor data, Phys. Rev. ST Accel. Beams **17**, 074001 (2014).

[20] M. Benedikt, F. Schmidt, R. Tomás, P. Urschütz, and A. Faus-Golfe, Driving term experiments at CERN, Phys. Rev. ST Accel. Beams **10**, 034002 (2007).

[21] B. Wei, Z. Bai, J. Tan, L. Wang, and G. Feng, Minimizing the fluctuation of resonance driving terms in dynamic aperture optimization, Phys. Rev. Accel. Beams **26**, 084001 (2023).

[22] B. Wei, Z. Bai, G. Feng, A. Loulergue, L. S. Nadolski, and R. Nagaoka, Analysis of off-momentum nonlinear driving terms for enlarging off-momentum dynamic apertures, Phys. Rev. Accel. Beams **27**, 104001 (2024).

[23] M. Xiao, Phase trombone program migration for the Recycler Ring at Fermilab, in *Proceedings of the IEEE Particle Accelerator Conference, Knoxville, TN, USA* (IEEE, Piscataway, NJ, 2005), pp. 3135–3137, https://ieeexplore.ieee.org/document/1591389.

[24] J. Zagel, M. Alvarez, B. Fellenz, C. Jensen, C. Lundberg, E. McCrory, D. Slimmer, R. Thurman-Keup, D. Tinsley, and J. Zagel, Third generation residual gas ionization profile monitors at Fermilab, in *Proceedings of the 3rd International Beam Instrumentation Conference (IBIC2014), Monterey, CA, USA* (2014), pp. 408–411, https://proceedings.jacow.org/IBIC2014/papers/tupd04.pdf?n=IBIC2014/papers/tupd04.pdf.

[25] R. Bartolini and F. Schmidt, Normal form via tracking or beam data, Part. Accel. **59**, 93 (1998), https://cds.cern.ch/record/333077.

[26] CERN, MAD-X: Methodical accelerator design, http://madx.web.cern.ch/madx.

[27] M. Xiao, Recycler chromaticities and end shims for NOvA at Fermilab, arXiv:1301.6666.

[28] R. Tomas Garcia. Direct measurement of resonance driving terms in the Super Proton Synchrotron (SPS) of CERN using beam position monitors, Ph.D. thesis, Universitat de Valencia, Valencia, Spain, 2003.

[29] M.-J. Yang, Lattice function measurement with TBT BPM data, Technical Report No. FERMILAB-TM-1922, Fermilab, 1996, https://lss.fnal.gov/archive/test-tm/1000/fermilab-tm-1922.pdf.

[30] J. Laskar, The chaotic motion of the solar system: A numerical estimate of the size of the chaotic zones, Icarus **88**, 266 (1990).

[31] F. Schmidt and R. Bartolini, SUSSIX: A computer code for frequency analysis of nonlinear betatron motion, https://cds.cern.ch/record/702438/files/sl-note-98-017.pdf (2023).

[32] G. Iadarola *et al.*, Xsuite: An integrated beam physics simulation framework, in *Proceedings of the HB2023, Geneva, Switzerland* (JACoW, Geneva, Switzerland, 2024), TUA2I1, 10.18429/JACoW-HB2023-TUA2I1.

[33] A. W. Chao and M. Month, Particle trapping during passage through a high-order nonlinear resonance, Nucl. Instrum. Methods **121**, 129 (1974).

[34] A. I. Neishtadt, Probability phenomena due to separatrix crossing, Chaos **1**, 42 (1991).

[35] G. Franchetti and I. Hofmann, Particle trapping by nonlinear resonances and space charge, Nucl. Instrum. Methods Phys. Res., Sect. A **561**, 195 (2006).

[36] S. Zhang, Calculation of incoherent space charge tune spread, AGS/AD/Tech Note No. 449, Brookhaven National Laboratory, 1996, https://technotes.bnl.gov/PDF?publicationId=30778.

[37] E. Benedetto, J. Abelleira, C. Bracco, V. Forte, B. Mikulec, and G. Rumolo, CERN PS booster upgrade and LHC beams emittance, in *Proceedings of the 6th International Particle Accelerator Conference (IPAC'15), Richmond, VA, USA* (JACoW, Geneva, Switzerland, 2015), pp. 3897–3900, 10.18429/JACoW-IPAC2015-THPF088.

[38] S. Papadopoulou, F. Antoniou, T. Argyropoulos, M. Hostettler, Y. Papaphilippou, and G. Trad, Impact of non-Gaussian beam profiles in the performance of hadron colliders, Phys. Rev. Accel. Beams **23**, 101004 (2020).

[39] T. Prebibaj, Optimization of the high brightness beam performance of the CERN PSB with H- injection, https://repository.cern/records/af762-j1w60 (2023), presented November 13, 2023.

[40] S. Umarov, C. Tsallis, and S. Steinberg, On a q-central limit theorem consistent with nonextensive statistical mechanics, Milan J. Math. **76**, 307 (2008).

[41] I. Hofmann, Comment on "Empirical condition of betatron resonances with space charge", Phys. Rev. Accel. Beams **23**, 028001 (2020).

[42] I. Hofmann, Coherent and incoherent space charge resonance effects, CERN Yellow Rep. Conf. Proc. **9**, 230 (2020).

[43] I. Hofmann, *Space Charge Physics for Particle Accelerators*, 1st ed., Particle Acceleration and Detection (Springer, Cham, 2017), p. 154, 10.1007/978-3-319-62157-9.

[44] K.-Y. Ng, *Physics of Intensity Dependent Beam Instabilities* (World Scientific, Singapore, 2006), p. 776.

[45] R. Baartman, Betatron resonances with space charge, AIP Conf. Proc. **448**, 56 (1998).

[46] C. Gonzalez-Ortiz, R. Ainsworth, and P. Ostroumov, Mitigation of third order resonances in the Fermilab recycler ring, 10.5281/zenodo.18166808 (2026).